

Research Article

Assimilation of MWHS-2/FY-3C 183 GHz Channels Using a Dynamic Emissivity Retrieval and Its Impacts on Precipitation Forecasts: A Southwest Vortex Case

Keyi Chen ¹, Jiao Fan ^{1,2}, and Zhipeng Xian ^{1,3}

¹School of Atmospheric Sciences, Chengdu University of Information Technology, Chengdu, China

²Meteorological Observatory, Guangxi Meteorological Administration, Nanning, China

³International Center for Climate and Environment Sciences, Institute of Atmospheric Physics, Chinese Academy of Sciences, Beijing, China

Correspondence should be addressed to Keyi Chen; ckydlt@aliyun.com

Received 21 February 2020; Revised 8 January 2021; Accepted 11 February 2021; Published 27 February 2021

Academic Editor: Stefano Dietrich

Copyright © 2021 Keyi Chen et al. This is an open access article distributed under the Creative Commons Attribution License, which permits unrestricted use, distribution, and reproduction in any medium, provided the original work is properly cited.

The dynamic emissivity retrieved from window channels of the microwave humidity sounder II (MWHS-2) onboard the China Meteorological Administration's FengYun (FY)-3C polar orbiting satellite can provide more realistic emissivity over lands and potentially improve the numerical weather prediction (NWP) forecasts. However, whether the assimilation with the dynamic emissivity works for the precipitation forecasts over the complex geography is less investigated. In this paper, a typical precipitating case generated by the Southwest Vortex is selected and the Weather Research and Forecasting data assimilation (WRFDA) system is applied to examine the impacts of assimilating MWHS-2/FY-3C with the uses of the emissivity atlas and the dynamic emissivity on the forecasts. The results indicate that the use of the dynamic emissivity retrieved from the 89 GHz channel of MWHS-2/FY-3C apparently increases the used data number for assimilation and does improve the initial fields and the 24-hour forecasts (from 0000 UTC 24 June 2016 to 0000 UTC 25 June 2016) of precipitation distribution and intensity except for the rainfall over 100 mm. But these positive impacts are not evidently better than those with the emissivity atlas. In general, these results still suggest that the future use of the dynamic emissivity in the assimilation over the complex terrain is promising.

1. Introduction

Satellite observation system can provide large quantity observations with high temporal and spatial resolution under all-sky conditions [1], which greatly compensate the sparse observations over oceans and plateaus [2]. With significant improvements in data assimilation algorithm and radiative transfer model, direct assimilation of satellite data has been widely adopted in the numerical weather prediction (NWP) centers and apparently improves the initial atmospheric fields (e.g., temperature, relative humidity, and wind vectors) and the forecasts of high-impact weather processes (e.g., heavy rainfall [3, 4]).

Compared with relatively smooth surface over the open ocean, over land and sea ice, the uncertainties in surface temperature and emissivity are higher and the cloud

screening is less effective, which makes it more difficult to assimilate microwave observations. Chen et al. [5] compared an approach in which the emissivity is retrieved dynamically from MWHS/FY-3B channel 1 (150 GHz (V)) with the use of an evolving emissivity atlas from 89 GHz observations from the Microwave Humidity Sounders (MHS) on NOAA and EUMETSAT satellites. This study found that the assimilation of the extra data over land with the dynamic emissivity employed improves the fitting of the short-range forecasts to other observations, and the forecasting impacts are mainly neutral to slightly positive over the first 5 days. Recently, the European Centre for Medium-Range Weather Forecasts (ECMWF) has assimilated the observations from FY-3C Microwave Humidity Sounders-2 (FY-3C MWHS-2), which is the second generation of the MWHS/FY-3A & B, in the operational forecasting system since April 4th, 2016 [6].

The Southwest Vortexes (SWVs), a kind of mesoscale cyclonic vortexes, occurring more over the Sichuan Basin and the southeast flank of the Tibetan Plateau (100°E~108°E, 26°N~33°N) at 850 hPa or 700 hPa isobaric level [7, 8], are generated by the interactions among the leeward slopes of the east-side terrain of the Qinghai-Tibet Plateau, Hengduan Cordillera, Sichuan Basin, and the multiscale atmospheric circulations [9, 10]. Migratory SWVs mainly move along either an eastward or southeastward path and the subtropical high is a key factor in determining its direction [11, 12]. Meanwhile, moisture transport provides more energy to support the development of SWVs along their trajectories, especially the moisture carried by the Indian Monsoon [11, 13]. SWVs produce intense precipitation along the way when they move downstream, affecting Sichuan, Chongqing, South China, North China, and the middle and lower reaches of the Yangtze River, which is the most characteristic precipitating phenomenon in China [7, 14–16]. Due to its great intensity and adverse impacts on the safety of the human life and social production, SWVs have been considered as the second most important storm system after the remnant low pressure of typhoon over land [17, 18].

These previous researches mainly used conventional observations, satellite images, and reanalysis data to conduct the diagnostic analysis and numerical simulations on the SWVs. However, there are few studies to evaluate the impacts of assimilating satellite observations, especially FengYun-3 (FY-3) series satellite observations from China Meteorological Administration, on the SWV forecasts. The complex terrain, that is, the Southwest China, always increases the uncertainties and difficulties of forecasts. Sichuan Basin is characterized by a complex terrain with hillock and mountainous areas surrounded as well as broad areas of farmland located. In addition, the northeast trending 500 km long Longmenshan margin marks the eastern border of the Tibetan Plateau with a horizontal distance of 50–100 km from the floor of the western Sichuan Basin to the eastern edge of the Tibetan Plateau [19]. Therefore, it is much interesting to investigate the impacts of assimilating MWHS-2/FY-3C observations by employing the dynamic emissivity on the forecasts of precipitation generated by the SWVs over the complex terrain. Dozens of assimilation experiments for precipitation forecasts of the SWVs have been conducted and neutral to slightly positive impacts are found in all of them. Therefore, a typical SWV case that occurred from 23 June 2016 to 25 June 2016 is selected as an example in this study, which caused heavy precipitation and affected most areas of the Sichuan Basin. 24-hour accumulated heavy precipitation (100–200 mm) was observed on 24 June 2016 in some regions and the next 24-hour weather report (25 June 2016) suggested that the south and northeast of the Sichuan Basin and Chongqing still had heavy rain. Severe weather phenomena, like hailstorms, strong winds, and thunderstorms, did occur with heavy rainfall causing huge economic losses to local residents. The data and methodology applied in this study are firstly introduced in Section 2. Experiment settings are described in Section 3, and results and discussion are presented in Section 4 before drawing conclusions in Section 5.

2. Data and Methodology

2.1. MWHS-2/FY-3C Observations. The first MWHS-2 instrument, flown on the Chinese FengYun-3C satellite, combines 5 traditional 183 GHz humidity sounding channels with novel channels around 118 GHz, which provides further information on temperature and clouds, and two window channels of 89 GHz and 150 GHz. The observations with good quality have been assimilated operationally since 5 April 2016 in ECMWF system [5]. The full list of the characteristics of the MWHS-2/FY-3C channels is displayed in Table 1. Note that in this study only the 183 GHz channels are used in assimilation with applying the 89 GHz window channel for emissivity retrievals over land and the 150 GHz channel for cloud screening.

2.2. WRFDA and Emissivity Retrieval. The WRFDA system and its three-dimensional variational (3D-VAR) component [20] are used in this study, which aims to obtain a statistically optimal analysis through an iterative minimization of a prescribed cost function:

$$J(\mathbf{x}) = \frac{1}{2}(\mathbf{x} - \mathbf{x}_b)^T \mathbf{B}^{-1}(\mathbf{x} - \mathbf{x}_b) + \frac{1}{2}(\mathbf{y} - H(\mathbf{x}))^T \mathbf{R}^{-1}(\mathbf{y} - H(\mathbf{x})), \quad (1)$$

where \mathbf{x} represents the atmospheric state vector, \mathbf{x}_b represents the background state, H represents the nonlinear observation operator that maps the model variables to the observation space, and \mathbf{y} represents the observation vector. For satellite radiance data assimilation, the RTTOV is applied as observation operator to simulate brightness temperatures. \mathbf{B} and \mathbf{R} represent the background and observation error covariance matrices, respectively. The NMC method [21] is employed to obtain case-dependent background error covariance matrices.

The complex surface geography largely affects the microwave signal emitted by land surfaces. Compared to 150 GHz channel, the 89 GHz channel is more sensitive to the lower latitudes [6] which cover the Sichuan Basin and other complex terrains, so that the latter is used for emissivity retrieval under the clear-sky conditions. One of the benefits to carry out an emissivity retrieval, rather than use an atlas, is that retrieved emissivity shows variability from one overpass to the next, which is more realistic.

According to Liu et al. [22], for a nonscattering plane-parallel atmosphere, assuming a flat and specular surface for a given zenith (θ) angle and frequency (ν), the TB (T_b) observed by a satellite sensor can be expressed as follows:

$$T_b = \varepsilon_{(\theta,\nu)} T_s \Gamma_{(\theta,\nu)} + (1 - \varepsilon_{(\theta,\nu)}) T_{(\theta,\nu)}^{\downarrow} \Gamma_{(\theta,\nu)} + T_{(\theta,\nu)}^{\uparrow}, \quad (2)$$

where $\varepsilon_{(\theta,\nu)}$ represents the surface emissivity at the observation zenith angle θ and frequency ν ; T_s , $T_{(\theta,\nu)}^{\downarrow}$, and $T_{(\theta,\nu)}^{\uparrow}$ represent the surface skin temperature obtained directly from the first guess, atmospheric downwelling radiation at the surface, and upwelling radiation at the top of the atmosphere, which are calculated within the RTTOV, respectively; and $\Gamma_{(\theta,\nu)}$ represents the net atmospheric

TABLE 1: The characteristics of MWHS-2/FY-3C.

Channel number	Central frequency (GHz)	FOVs	Peak of the weighting function (hPa)	Swath width (km)	Horizontal resolution (km)
1	89 (H)		—		
2	118.75 ± 0.08 (V)		20		
3	118.75 ± 0.2 (V)		60		
4	118.75 ± 0.3 (V)		100		
5	118.75 ± 0.8 (V)		250		25
6	118.75 ± 1.1 (V)		300		
7	118.75 ± 2.5 (V)	98	700	2700	
8	118.75 ± 3.0 (V)		—		
9	118.75 ± 5.0 (V)		—		
10	150 (H)		—		
11	183 ± 1.0 (V)		350		
12	183 ± 1.8 (V)		400		
13	183 ± 3.0 (V)		500		16
14	183 ± 4.5 (V)		550		
15	183 ± 7.0 (V)		650		

transmissivity. The emissivity can be retrieved from the following equation:

$$\varepsilon_{(\theta,\nu)} = \frac{T_b - (T_{(\theta,\nu)}^\uparrow + T_{(\theta,\nu)}^\downarrow)\Gamma_{(\theta,\nu)}}{(T_s - T_{(\theta,\nu)}^\downarrow)\Gamma_{(\theta,\nu)}}. \quad (3)$$

The retrieved surface emissivity is used only under the conditions when the surface-to-space transmittance for 89 GHz is larger than 0.5 and when the difference between the retrieved emissivity and the equivalent value from the Tool to Estimate Land Surface Emissivity at Microwaves and Millimeter (TELSEM) waves atlas is less than 0.2. Otherwise, the TELSEM atlas value for the corresponding channels is used.

2.3. Quality Control. Before any process begins, the MWHS-2/FY-3C observations are thinned to a spacing of 60 km. Other quality control procedures [23] include the following: remove observations with brightness temperature lower than 50 K or larger than 550 K; remove pixels with mixed surface types; remove the first five scan angles over the swath edges according to the evaluation report of MWHS-2/FY-3C [24]; and remove the observations if the bias corrected normalized innovation (O-B) exceeds 3σ , where σ represents the specified standard deviation in the observation error. Over land, the orography check is also important to avoid observations that are too sensitive to the surface, that is, where errors in the surface emissivity or the skin temperatures play a large role. The threshold of the orography for

channel 11 is 1500 m; that for channels 12-13 is 1000 m; and that for channels 14-15 is 800 m for MWHS-2/FY-3C. These thresholds reflect the different surface sensitivities of the sounding channels, that is, more rigorous for the lowest channels (channels 14-15) and less tight for the higher channels [6].

To remove observations strongly affected by ice cloud and precipitation, a 5 K check on the absolute value of the first-guess departure of channel 10 (150 (V) GHz) is employed [6]. This definition of “clear sky” will be used in this paper: it does not mean no clouds; rather the radiative impact of clouds is considered to be small and is not analyzed. Note that this criterion will also reject data for which the emissivity or skin temperature estimate is significantly in error. A variational bias correction scheme, known as VarBC [25, 26], is also applied to remove the systematic errors. Figure 1 shows the probability distribution function (PDF) of the first guess departures of the MWHS-2/FY-3C channels 11–15 at 0000 UTC 23 June 2016 before and after VarBC. Apparently, after VarBC, the PDFs shift more towards zero to meet the requirements of the data assimilation algorithms for unbiased error models.

3. Experimental Settings

According to the characteristics of the trajectories, the southwest vortexes can be categorized into the local type and the moving type. The latter can be further divided into the eastward-trajectory type, the northeastward-trajectory type, and the southeastward-trajectory type. For the local type, the southwest vortexes rarely move out and the affected regions are small. Meanwhile, for the moving type, the vortexes can move eastward, northeastward, or southeastward, having a great influence on broad areas and even merging into other weather systems [12].

One typical local type case occurring from 23 June to 25 June 2016 mentioned in Section 1 is selected to show the assimilating impacts by using dynamic emissivity on the forecasts of heavy rainfall in this study. Three experiments were conducted as follows: the first experiment (denoted as CN) does not conduct data assimilation; the second (denoted as AL) and the third (denoted as DY) experiments both assimilate MWHS-2/FY-3C clear radiances, with the former using emissivity atlas and the latter using dynamic emissivities. The Advanced Research WRF (ARW) version 3.8 modeling system and the 3D-VAR component of the WRFDA are applied. Euler mass coordinates and the Runge–Kutta 3rd-order time integration option are used. The model configuration includes 320×270 grid points, with a horizontal resolution of 15 km, 30 eta levels in the vertical direction, and a model top level at 10 hPa. The time step is 60 seconds, while the forecast interval is 12 hours. The physical parameterization schemes used in all experiments are displayed in Table 2. The assigned observation errors over land are also listed in Table 2 based on the two-month (May and June 2016) statistics of innovation (observation minus background, O-B) [27, 28].

The model integration time is from 0000 UTC 23 June 2016 to 0000 UTC 25 June 2016 in the three experiments,

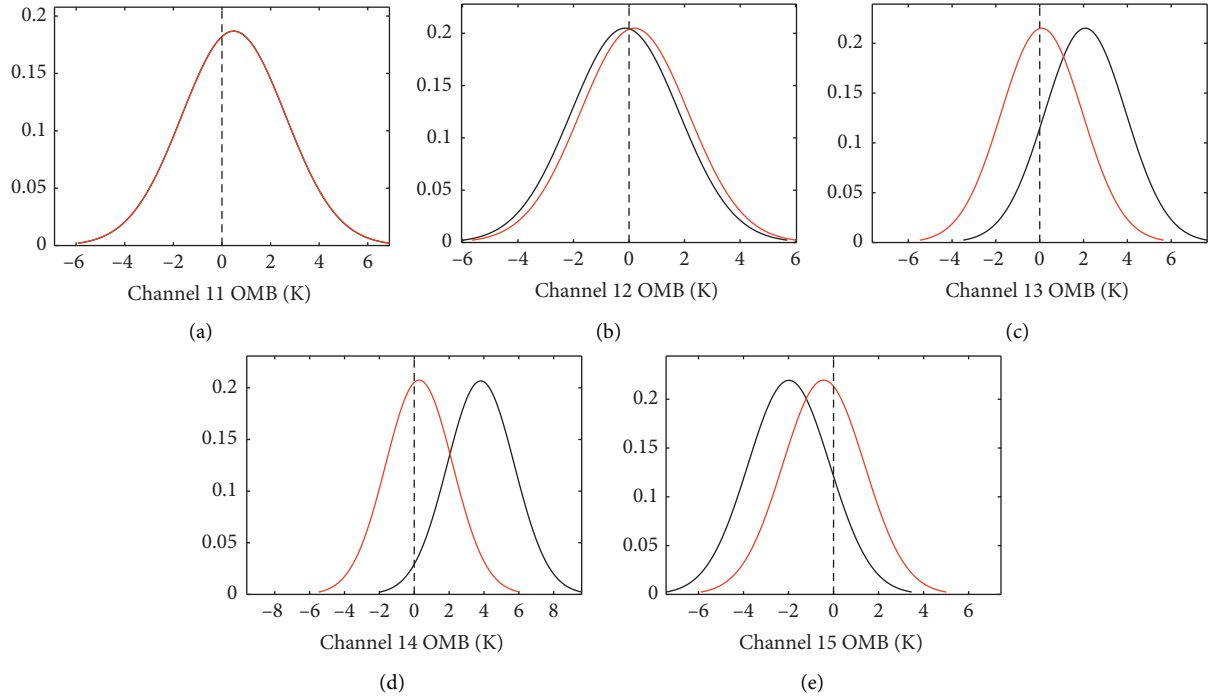


FIGURE 1: The PDF of the first-guess departures of the MWHS-2/FY-3C observations of channels 11–15 (a–e) at 0000 UTC 23 June 2016 before (black line) and after (red line) VarBC.

and the cycling forecast-analysis experiments of assimilating MWHS-2 observations every 12 hours are carried out. The analyses are generated every 12 hours in the cycling experiments. The background is a 12-hour WRF forecast initialized from the previous cycle's analysis except that the background for the first analysis is the forecast initiated from the final (FNL) global analysis data (resolution: $1^\circ \times 1^\circ$) at 1200 UTC 22 June 2016. The assimilating time window is 6 hours and the observation data within ± 3 hours of the analysis time are selected and assumed to be valid at the analysis time.

4. Results and Discussion

4.1. The Usage of the MWHS-2 Observations. To examine the impact of the technical implementation of emissivity retrieval, the usage of the MWHS-2 observations is investigated. During the whole assimilation period (i.e., from 0000 UTC 23 June to 1200 UTC 24 June), the amount of the used data in the DY experiment is greater than that in the AL experiment (Table 3). Note that, compared with channels 12–15, more MWHS-2 observations from channel 11 are assimilated as its peak height is higher and it is less affected by the complex surface geography. On the other hand, as shown in Figures 2(a) and 2(b), the MWHS-2 observations are mainly distributed in central and southern China in the DY and AL experiments. However, over 10% extra observations from each channel in the DY experiment are regained (Table 4), meaning that the emissivity retrievals have a great ability to increase the usage of the MWHS-2

observations and more realistic emissivities are obtained. These extra observations mainly located in northern China; meanwhile, there are small parts of the observations over central and eastern China (Figures 2(c)–2(f)), which would provide more atmospheric information and have a potential to perform better on forecasts.

In order to evaluate the accuracy of the retrieved emissivity, the differences between the retrieved emissivity from 89 GHz channel of MWHS-2/FY-3C and the TELSEM atlas at 0000 UTC 23 June 2016 are displayed in Figure 3(c). The larger differences are distributed over hypsographic areas, which suggests that the retrieved emissivity is more variable and realistic than the TELSEM atlas.

4.2. Impacts of the Emissivity Retrievals on the Initial Fields. The PDFs of the first-guess departures of MWHS-2 observations from each channel during the whole assimilation period in the two experiments are shown in Figure 4. After employing the emissivity retrievals, the patterns of the PDFs in the DY experiment became relatively slimmer and higher as compared with the AL experiment, especially for channels 14–15, which suggests that the emissivity retrievals have an ability to improve the accuracy of the background obtained from the model.

As for the impact of emissivity retrievals on physical fields, the averaged root mean square error differences (Δ RMSE) between the analysis departures (O-A) and the first-guess departures (O-B) of the temperature, relative humidity, wind velocity, and geopotential height are calculated (Figure 5); that is,

TABLE 2: The employed physical parameterization schemes and assigned observation errors for MWHS-2/FY-3C.

Parameterization scheme	Configuration				
Microphysics scheme	Thompson scheme [29]				
Radiation scheme	RTTM short-wave and long-wave radiation schemes [30]				
Cumulus scheme	Tiedtke scheme [31, 32]				
Planetary boundary layer scheme	Mellor–Yamada–Janjic scheme [33]				
Land surface scheme	Unified Noah land surface model [34]				
MWHS-2/FY-3C observation error (K)					
Channel 11	Channel 12	Channel 13	Channel 14	Channel 15	
2.3	2.3	2.3	2.5	2.5	

TABLE 3: The percentage of the used data for channels 11–15 at each analysis time.

Channel number	0000 UTC 23 June		1200 UTC 23 June		0000 UTC 24 June		1200 UTC 24 June	
	AL	DY	AL	DY	AL	DY	AL	DY
11	44.19%	52.56%	46.30%	55.12%	46.23%	53.44%	47.15%	54.41%
12	42.87%	46.01%	38.53%	41.89%	45.80%	49.62%	38.44%	43.53%
13	43.76%	47.02%	38.93%	42.33%	46.99%	50.81%	38.59%	44.28%
14	42.13%	43.76%	36.67%	38.77%	45.65%	48.14%	35.82%	41.01%
15	42.25%	43.91%	37.15%	39.54%	45.85%	48.28%	36.37%	41.16%

$$\text{RMSE} = \sqrt{\frac{1}{N} \sum_{i=1}^N (y_{io} - y_{if})^2}, \quad (4)$$

$$\text{delta RMSE} = \text{RMSE}_{\text{O-A}} - \text{RMSE}_{\text{O-B}}, \quad (5)$$

where N is the number of model grids, y_{io} and y_{if} denote the i th observation from ECMWF ERA-5 analysis and i th data from the analysis or first guess in the two experiments, respectively. Negative values indicate positive impacts. Figure 5 shows not only the impacts of data assimilation on the physical fields in the two experiments and the impacts of the emissivity retrievals employed in the DY experiment on the physical fields as compared with the AL experiment but also which levels reflected the positive impacts. An apparently positive impact has been reflected in temperature and relative humidity in the AL and DY experiments (Figures 5(a) and 5(b)). For the wind velocity and geopotential height as well as mid-low-level relative humidity, negative impacts are detected in the two experiments (Figures 5(b)–5(d)). The reasons for these negative impacts are not clearly, but some studies [35, 36] have also addressed this situation. They indicated that other advanced data assimilation approaches, such as hybrid (ensemble/3D-VAR) or 4D-VAR method, will deal with this problem as these advanced data assimilations can provide flow-dependent ensemble background covariance error which is not achieved in the 3D-VAR data assimilation. Note that these negative impacts are relatively smaller in the DY experiment as the absolute values of the RMSE differences are smaller than those in the AL experiment, especially the mid-low-level wind velocity and low-level relative humidity.

On the other hand, the impacts of emissivity retrievals on each channel are shown in Table 5. Generally, the mean and

standard deviation of analysis departures are smaller than those of first-guess departures. The values of mean and standard deviation of the first-guess and analysis departures in the AL and DY experiments are nearly the same, but the number of observations assimilated in the DY experiment is greater than that in the AL experiment. In addition, the variations of values in the DY experiment during the whole assimilation period are slight, suggesting that the extra observations in the DY experiment let through by QC procedures might reinforce model biases.

4.3. Impacts of the Precipitation Forecasts. There was a band of water vapor flux ($>12 \text{ g hPa}^{-1} \text{ cm}^{-1} \text{ s}^{-1}$) over the Yangtze River in the ERA-5 analysis obtained from the ECMWF (Figure 5(a)), and the moisture was transported from Southwestern China to Eastern China. The band of maximum water vapor flux was nearly east-west direction in the ERA-5 analysis, while in the CN, AL, and DY experiments, the direction was northeast-southwest (Figure 5). In addition, there were two maximum water vapor flux centers ($>18 \text{ g hPa}^{-1} \text{ cm}^{-1} \text{ s}^{-1}$) over the band in the ERA-5 analysis, AL and DY experiments as compared with the CN experiment. However, the locations of two centers in the ERA-5 analysis were evidently different from the experiments assimilating the MWHS-2 observations. The translation speed of a cyclonical vortex (i.e., southwest vortex) located in the east of Sichuan Province in the ERA-5 analysis (Figure 6(a)) was not simulated successfully by the model (Figures 6(b)–6(d)).

The 24-hour accumulated precipitation from 0000 UTC 24 June to 0000 UTC 25 June 2016 is shown in Figure 7. The distribution of precipitation was east-west direction (Figure 7(a)), which was the same as the band of water vapor flux as discussed above. The heavy rainfall

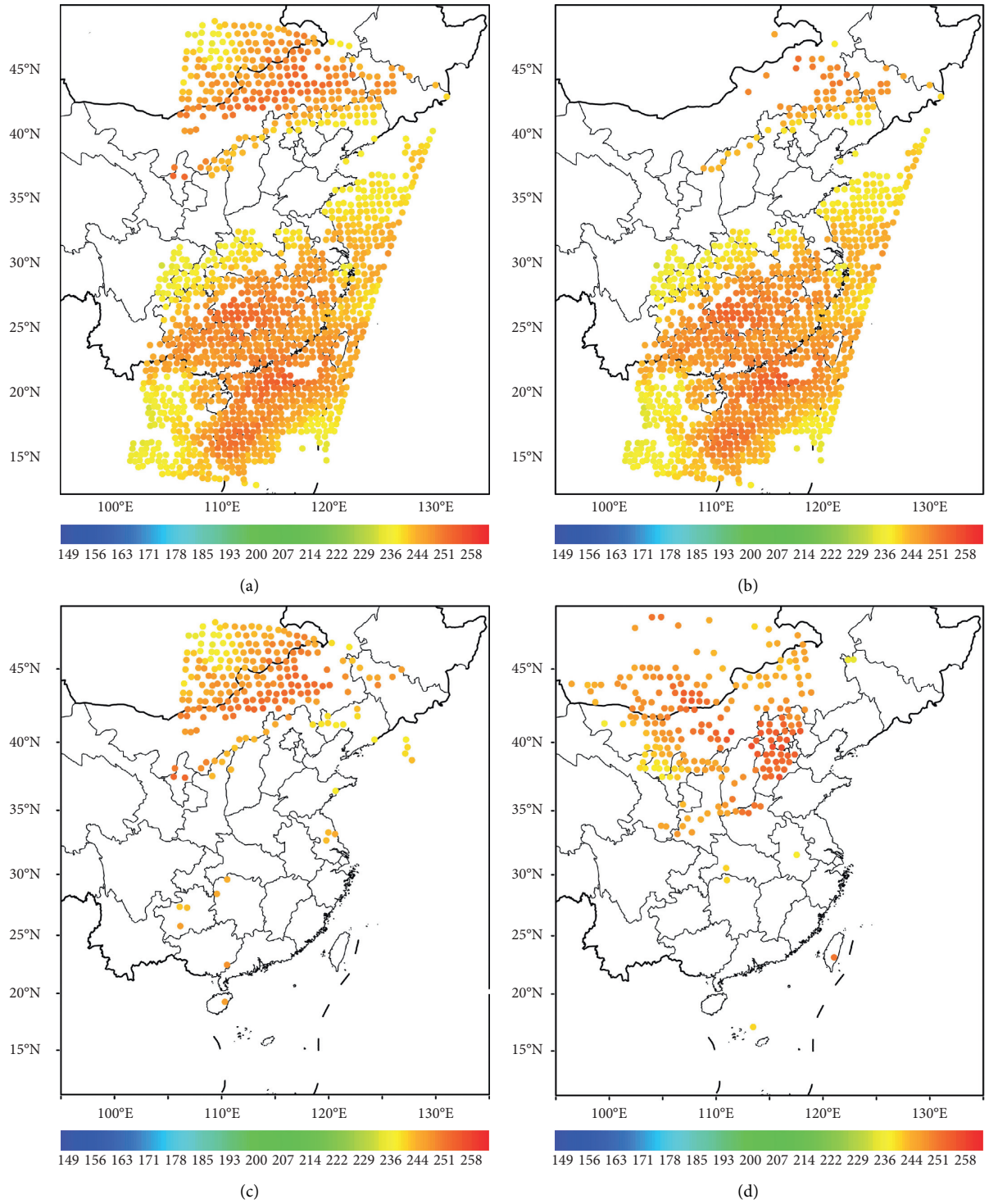


FIGURE 2: Continued.

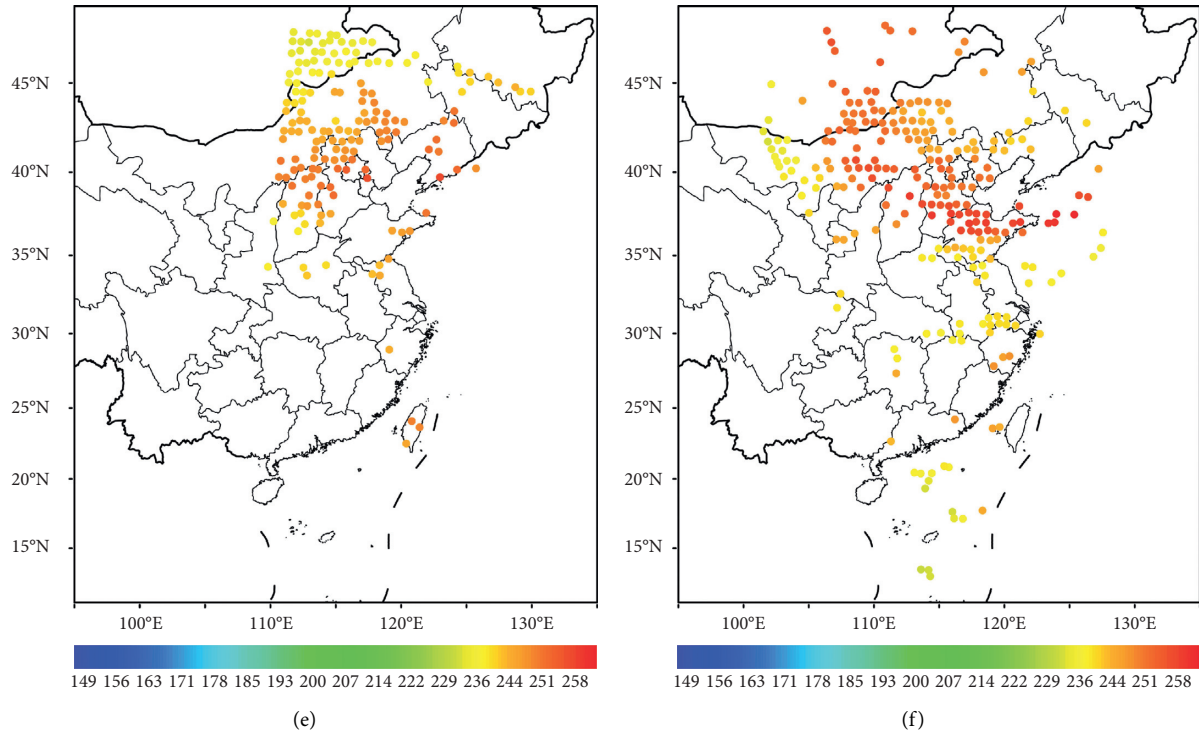


FIGURE 2: The distributions of the assimilated observations of channel 11 at 0000 UTC 23 June in the DY (a) and AL (b) experiments; the distributions of extra assimilated observations in the DY experiments at 0000 UTC 23 June (c), 1200 UTC 23 June (d), 0000 UTC 24 June (e), and 1200 UTC 24 June (f) (the dashed lines off the coast are the national boundaries of China over sea).

TABLE 4: The extra assimilated observations for channels 11–15 reobtained by the emissivity retrievals at each analysis time.

Channel	Date			
	0000 UTC 23 June (2580)	1200 UTC 23 June (2471)	0000 UTC 24 June (2094)	1200 UTC 24 June (1985)
11	386	452	299	367
12	355	323	281	253
13	361	321	293	261
14	331	291	265	220
15	332	300	268	224

The values in the brackets represent the total number of observations over the model domain in the AL and DY experiments.

(>100 mm) centers were mainly located in Sichuan and Chongqing Provinces in the observations. But in the CN experiment (Figure 7(b)) the amount of precipitation was overestimated, and the distribution of heavy rainfall was more spacious and moved eastward as compared with the observations, AL and DY experiments. The amount of heavy rainfall in the AL experiment (Figure 7(d)) was closer to the observations as compared with the DY experiment (Figure 7(c)), especially in the west of Guizhou Province and north of Hunan Province. The results of the equitable threat score (ETS) show that the two assimilation experiments made much better forecasts of precipitation as compared with the CN experiment except for the rainfall over 100 mm (Figure 8). The score of the precipitation over 100 mm in the CN experiment was slightly higher than the assimilation experiments, but the distribution of rainfall over 100 mm was more spacious than the observations and two assimilation experiments. In addition, the score results

from the AL experiment were better than those from the DY experiment; these can be also reflected by the forecasts of the temperature, humidity, wind, and geopotential height (Figure 9). The two experiments assimilating the MWHS-2 observations improved all the variables (i.e., temperature, relative humidity, wind velocity, and geopotential height) significantly as compared with the CN experiment. These improvements mainly occurred below 600 hPa, and the AL experiment made better performances compared to the DY experiment. So why the results from the dynamic emissivity (DY) experiment could not evidently improve the forecast even though there are some extra observations assimilated as compared with the emissivity atlas (AL) experiment is an obvious question needed to be answered. On one hand, the majority of extra observations are concentrated on the northeast of China, and there are few extra observations over the west-east rainfall band over the Yangtze River where the MWHS-2

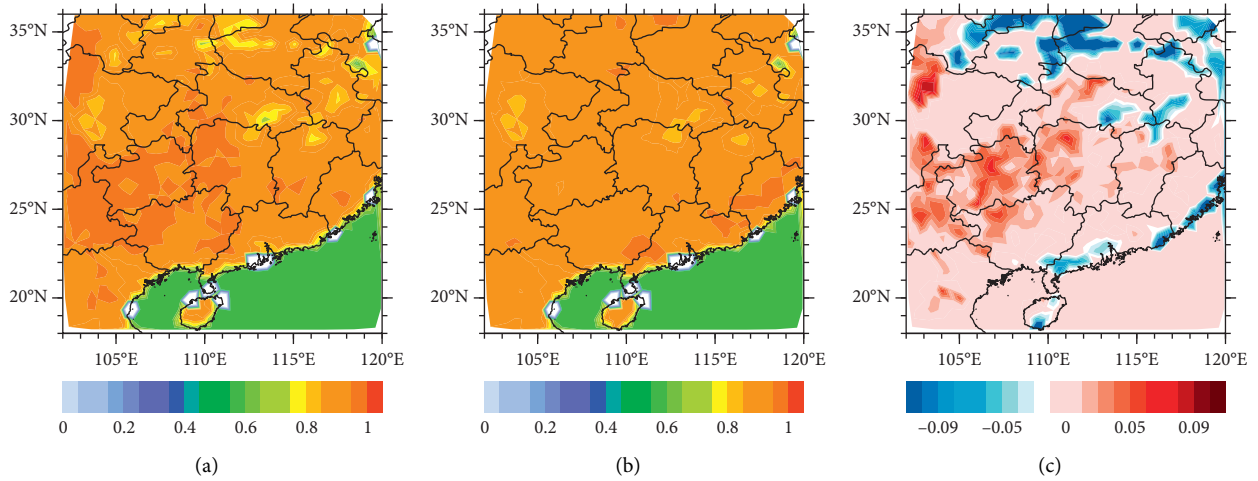


FIGURE 3: The emissivities from the clear sky (a), the TELSEM atlas (b), and the differences between the dynamic emissivity and the atlas (c) for MWHS-2/FY-3C after quality control at 0000 UTC 23 June 2016.

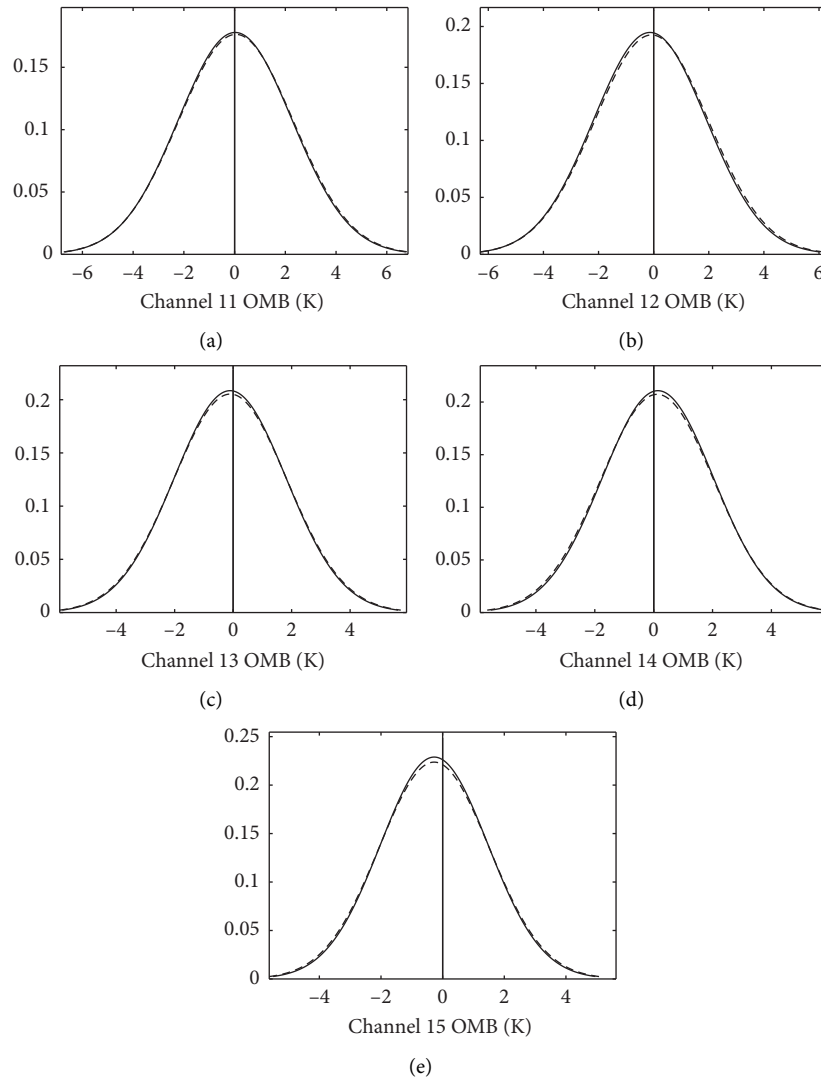


FIGURE 4: The PDF distributions of the first-guess departures of assimilated observations which are in the AL (dashed line) and DY (bold line) experiments from 0000 UTC 23 June to 0000 UTC 25 June for channels 11–15 (a–e).

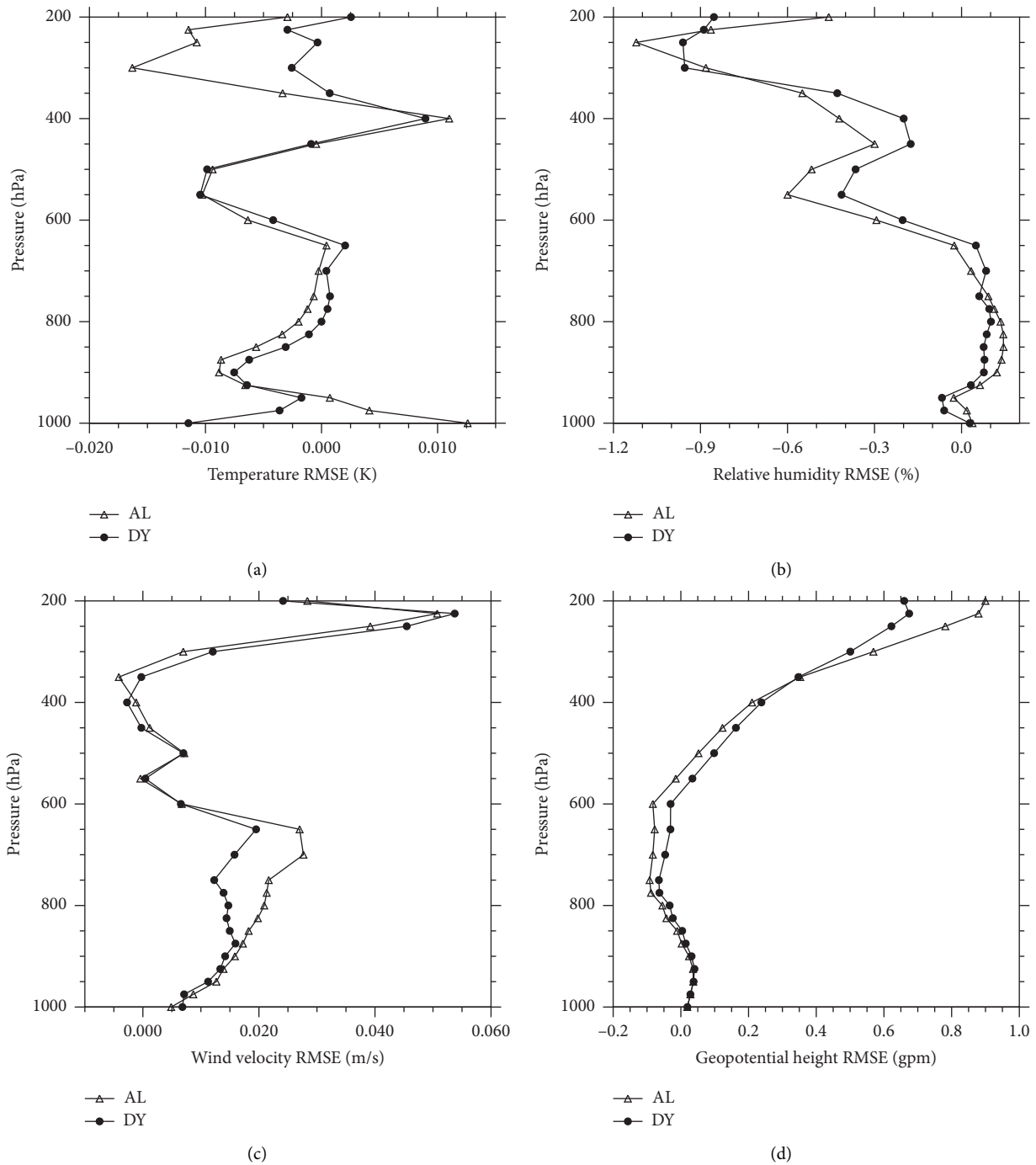


FIGURE 5: The vertical profiles of the averaged RMSEs differences between the analysis departures (O-A) and the first-guess departures (O-B) of the temperature (a) (unit: K), relative humidity (b) (unit: %), wind velocity (c) (unit: m/s), and geopotential height (d) (unit: gpm) from the AL (triangle line) and DY (circle line) experiments at 0000 UTC 23 June 2016.

observations are contaminated by the cloud/rain and excluded to satisfy the clear-sky criterion. On the other hand, it is more difficult to retrieve accurate real-time surface emissivity over the complex terrain (e.g., the southwest of China), where the skin temperatures vary dramatically, and the biases introduced by retrieving the emissivity would

increase the forecast errors, making the quality of forecast decreased. More work should be further carried out to solve the problem of emissivity retrievals over the complex and mixture terrain and the all-sky approach should be applied to effectively assimilate the cloud- and rain-affected observations.

TABLE 5: The mean and standard deviation of O-B and O-A and the number of assimilated observations for channels 11–15 in the AL and DY experiments at each analysis time.

MWHS-2/FY-3C channels	Mean (O-B)		Mean (O-A)		Std (O-B)		Std (O-A)		OBS Num	
	AL	DY	AL	DY	AL	DY	AL	DY	AL	DY
0000 UTC 23 June										
11	0.48	0.48	0.08	0.08	2.17	2.14	0.90	0.89	1140	1356
12	0.19	0.19	-0.06	-0.06	1.96	1.95	0.76	0.76	1106	1187
13	0.08	0.09	0.00	0.01	1.87	1.85	0.68	0.70	1129	1213
14	0.29	0.28	0.24	0.25	1.92	1.92	0.69	0.71	1087	1129
15	-0.42	-0.44	-0.21	-0.22	1.81	1.82	0.76	0.78	1090	1133
1200 UTC 23 June										
11	-0.02	-0.07	0.00	0.00	2.16	2.17	0.85	0.86	1144	1362
12	-0.18	-0.17	-0.07	-0.07	1.98	1.98	0.72	0.74	952	1035
13	-0.01	0.02	-0.01	0.01	1.82	1.84	0.70	0.71	962	1046
14	0.45	0.47	0.26	0.28	1.77	1.79	0.73	0.74	906	958
15	0.10	0.09	-0.05	-0.07	1.65	1.70	0.79	0.82	918	977
0000 UTC 24 June										
11	0.10	0.00	0.07	0.07	2.23	2.18	0.95	0.91	968	1119
12	0.01	-0.08	0.02	0.01	2.04	2.04	0.82	0.81	959	1039
13	-0.11	-0.18	0.00	0.00	1.88	1.87	0.73	0.74	984	1064
14	-0.01	-0.03	0.11	0.12	1.79	1.79	0.74	0.76	956	1008
15	-0.27	-0.32	-0.10	-0.11	1.71	1.71	0.80	0.80	960	1011
1200 UTC 24 June										
11	-0.44	-0.48	-0.02	-0.04	2.42	2.34	0.87	0.89	936	1080
12	-0.44	-0.58	0.04	0.00	2.31	2.18	0.80	0.83	763	864
13	-0.46	-0.43	0.05	0.05	2.21	2.07	0.77	0.82	766	879
14	-0.39	-0.22	0.15	0.19	2.15	2.00	0.83	0.88	711	814
15	-0.54	-0.43	-0.12	-0.12	1.91	1.67	0.86	0.87	722	817

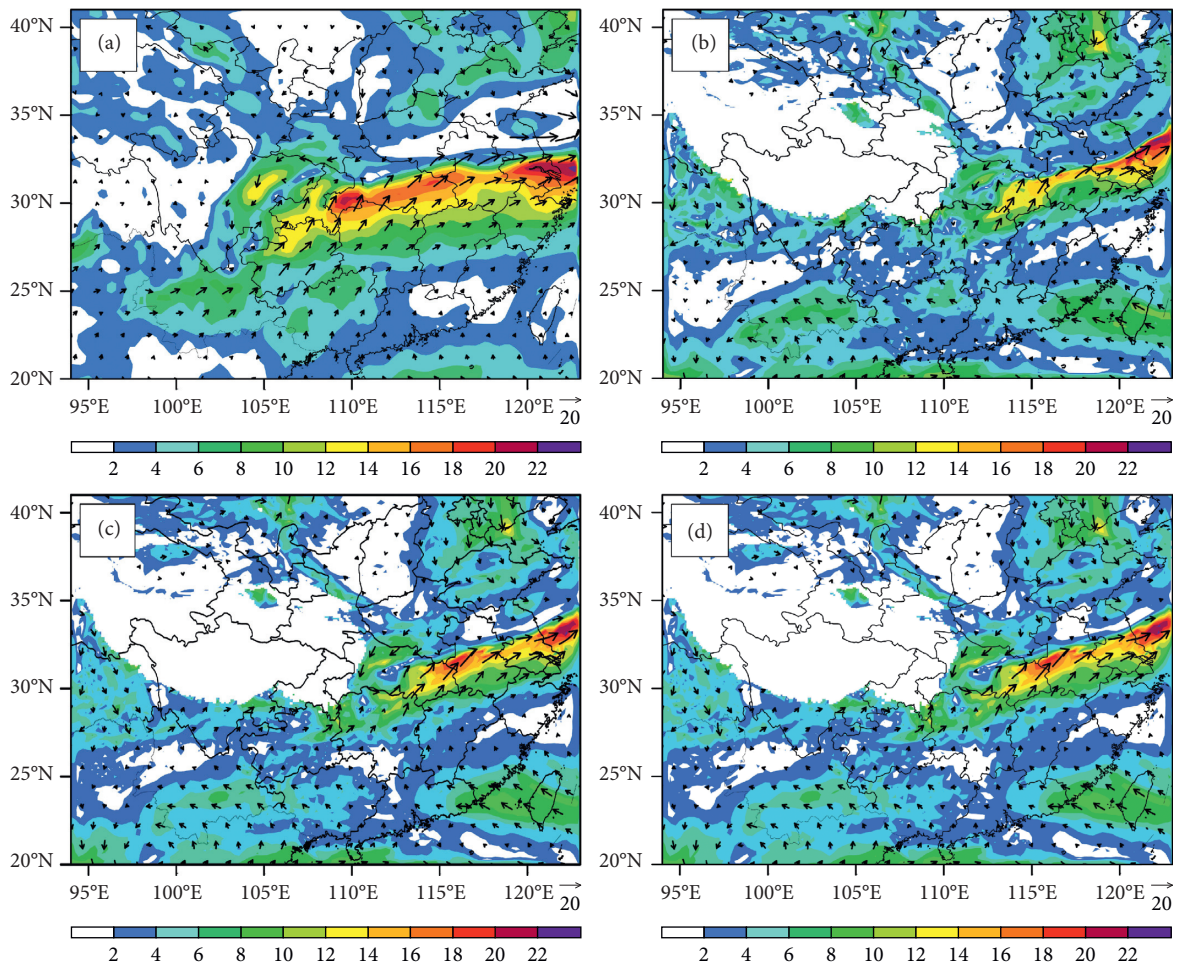


FIGURE 6: The 700 hPa water vapor flux (shaded; unit: $\text{g hPa}^{-1} \text{cm}^{-1} \text{s}^{-1}$) at 1200 UTC 24 June 2016 from the ERA-5 analysis (a), CN experiment (b), DY experiment (c), and AL experiment (d).

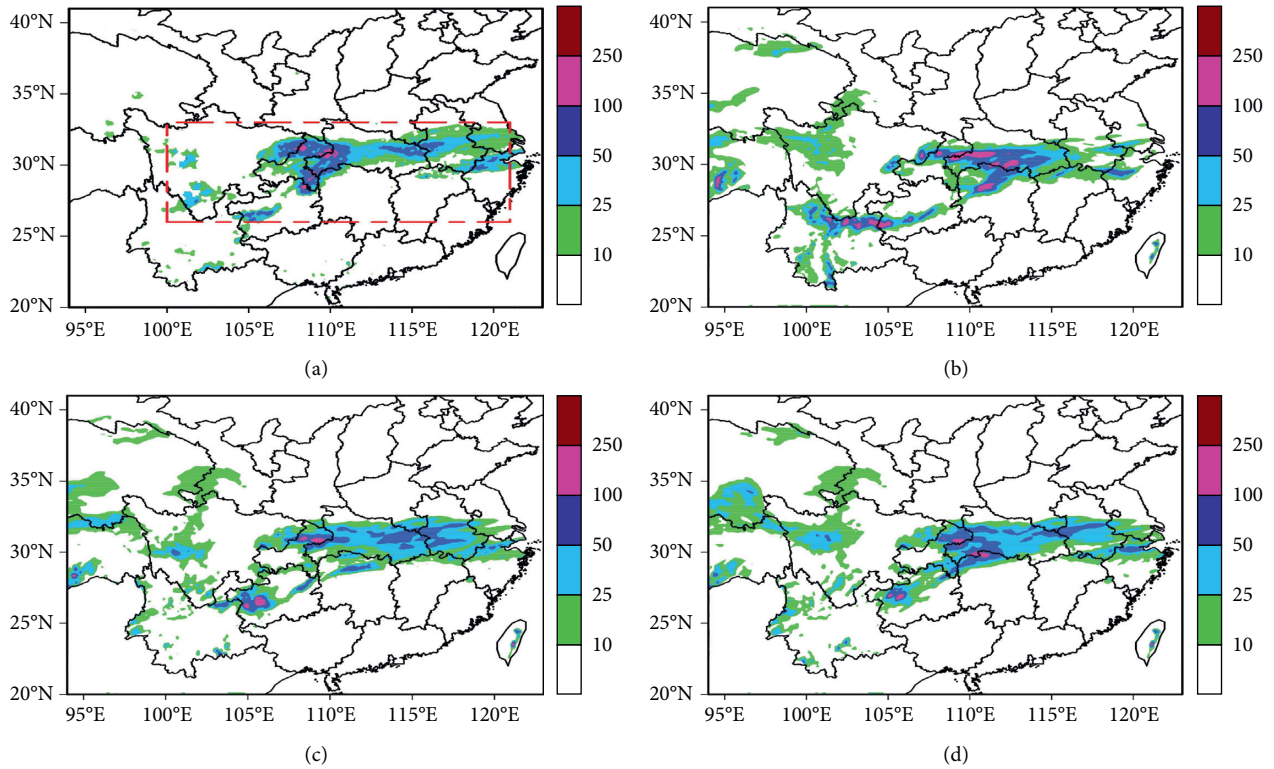


FIGURE 7: The 24-hour accumulated precipitation (unit: mm) from 0000 UTC 24 June 2016 to 0000 UTC 25 June 2016 from the hourly intensive automatic rainfall stations of the China Meteorological Administration observations (a), CN experiment (b), DY experiment (c), and AL experiment (d).

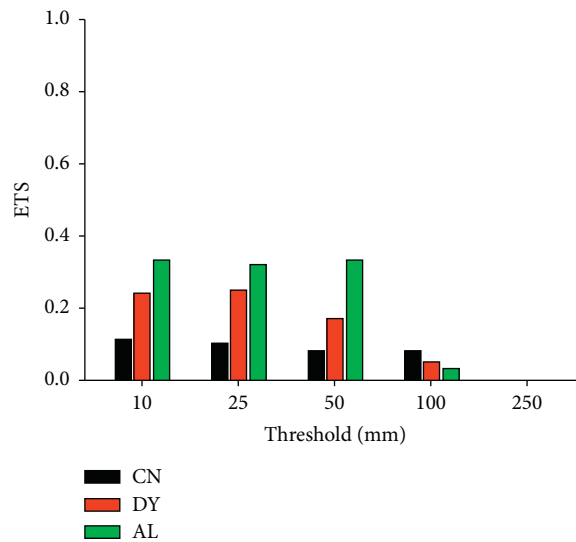


FIGURE 8: The ETSs of the 24-hour accumulated precipitation from 0000 UTC 24 June 2016 to 0000 UTC 25 June 2016 for the CN (black), DY (red), and AL (green) experiments at 10, 25, 50, 100, and 250 mm rainfall thresholds. The calculation area is the Yangtze River displayed in Figure 6(a) with a red-dashed line tangle.

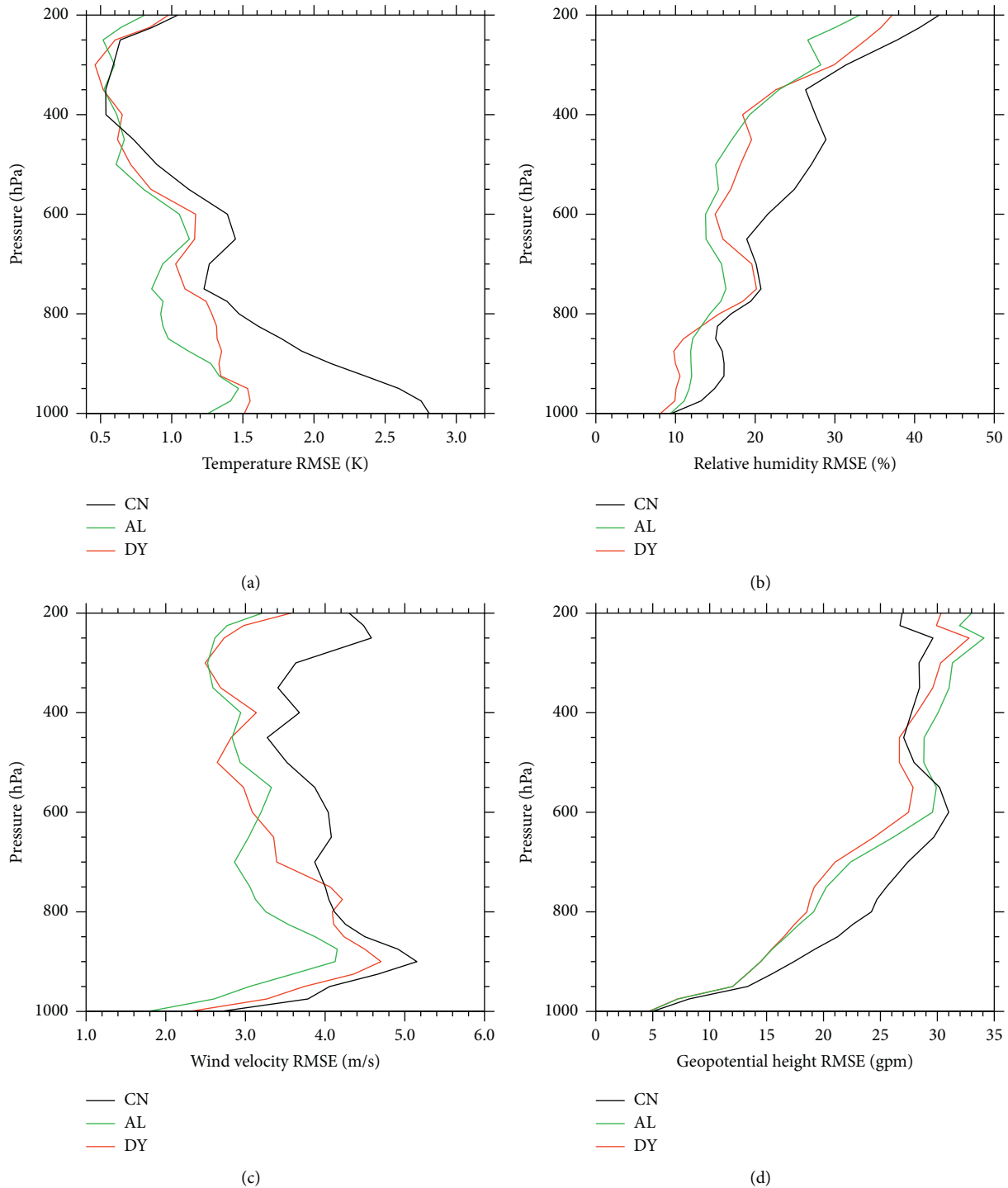


FIGURE 9: The vertical profiles of the 24-hour forecast RMSEs from 0000 UTC 24 June to 0000 UTC 25 June 2016 referring to the ERA-5 analysis of the temperature (a) (unit: K), relative humidity (b) (unit: %), wind velocity (c) (unit: m/s), and geopotential height (d) (unit: gpm) fields from the CN (black line), AL (green line), and DY (red line) experiments. The calculation area is the Yangtze River displayed in Figure 6(a) with a red-dashed line tangle.

5. Conclusions

In this study, the WRFDA system and its 3D-VAR scheme are employed to evaluate the impacts of assimilating MWHS-2/FY-3C with emissivity atlas and dynamic emissivity applied on the analysis and forecasts of precipitation

generated by a representative SWV case over complex terrain within a limited domain. Apparently, the dynamic emissivity could provide more accurate and detailed emissivity over lands and allow more MWHS-2/FY-3C observations to be assimilated. Mainly positive impacts are shown in the initial atmospheric fields, that is, temperature and

relative humidity, but some negative impacts are detected in the wind velocity and geopotential height as well as mid-low-level relative humidity.

For the precipitation forecasts, both 700 hPa water vapor flux and 24-hour accumulated precipitation from 0000 UTC 24 June to 0000 UTC 25 June 2016 indicate that the assimilation of MWHS-2/FY-3C observations undoubtedly can improve the precipitation forecast of the SWV and the precipitation distribution and intensity are closer to the observations, regardless of the uses of the emissivity atlas and the dynamic emissivity. The ETSs of the 24-hour accumulated precipitation and the vertical profiles of the 24-hour forecast RMSEs further verify these improvements. Apparently, assimilating MWHS-2/FY-3C data with the dynamic emissivity can increase the amount of assimilated data, but its impacts on this SWV precipitation forecast case are not evidently positive compared to the case with the emissivity atlas. The possible reasons may be the following: firstly, since the main changes in data usage are produced from the channels sensitive to the higher-level water vapor (i.e., channel 11), it is not surprising to see slight improvement for lower-level fields with the change of the assimilation strategy; secondly, the extra observations assimilated might reinforce model biases, which makes the results in the DY experiment not better than the AL experiment. Also, the quality control removes the cloud- and rain-contaminated observations and only clear-sky data that are assimilated in this study leading to quite a lot of important information are excluded. Therefore, all-sky assimilation (under clear, cloudy, and precipitating conditions) would be a useful approach to make good use of cloud- and rain-affected observations and further study with more SWV cases is also required to investigate the impacts of assimilating MWHS-2 observations on the SWV precipitation forecasts.

Data Availability

The FY radiance data were obtained freely from <http://fy3.satellite.cma.gov.cn>. The ERA-5 analysis can be downloaded from <https://apps.ecmwf.int/data-catalogues/era5/?class=ea>. The precipitation observations can be obtained from <http://data.cma.cn>.

Conflicts of Interest

The authors declare that they have no conflicts of interest.

Acknowledgments

The authors appreciate the National Natural Science Funds of China for supporting this research through Grant no. 41875039 and Chengdu University of Information Technology Project (Grant no. 2020H216) (the Software Development of Satellite Remote Sensing Monitoring Service for Road Transportation in Southwest Region of China (FengYun-3 Second Batch Meteorological Satellite Ground Engineering Application System)).

References

- [1] B. Zhang, L. F. Zhang, and C. H. Xiong, "Effects of ATOVS data assimilation schemes on the simulation of heavy rain," *Chinese Journal of Atmospheric Sciences*, vol. 38, no. 5, pp. 1017–1027, 2014, in Chinese.
- [2] T. Xue, Z. Y. Guan, J. J. Xu, and M. Shao, "The impact of ATMS and CrIS data assimilation on weather forecasts over the Qinghai-Tibetan Plateau," *Plateau Meteorology*, vol. 36, no. 4, pp. 912–929, 2017, in Chinese.
- [3] L. L. Qi, J. H. Sun, and X. L. Zhang, "The ATOVS data assimilating experiments on the heavy rain over the Yangtze river basin," *Chinese Journal of Atmospheric Sciences*, vol. 29, no. 5, pp. 780–794, 2005, in Chinese.
- [4] J. Li and G. F. Zhu, "Application analysis of direct assimilation of satellite radiation data on heavy rain forecasting," *Meteorological Monthly*, vol. 34, no. 12, pp. 36–43, 2008, in Chinese.
- [5] K. Chen, N. Bormann, S. English, and J. Zhu, "Assimilation of Feng-Yun-3B satellite microwave humidity sounder data over land," *Advances in Atmospheric Sciences*, vol. 35, no. 3, pp. 268–275, 2018.
- [6] H. Lawrence, F. Carminati, W. Bell et al., *An Evaluation of FY-3C MWRI and Assessment of the Long-Term Quality of FY-3C MWHS-2 at ECMWF and the Met Office*, ECMWF Technical Memoranda, Reading, UK, 2017.
- [7] J. H. Wang, D. L. Li, and Y. Wang, "Characteristics re-analysis on Southwest vortex," *Journal of the Meteorological Sciences*, vol. 35, no. 2, pp. 133–139, 2015, in Chinese.
- [8] X. Feng, C. Liu, G. Fan, X. Liu, and C. Feng, "Climatology and structures of southwest vortices in the NCEP climate forecast system reanalysis," *Journal of Climate*, vol. 29, no. 21, pp. 7675–7701, 2016.
- [9] Q. Wang and Z. Tan, "Multi-scale topographic control of southwest vortex formation in Tibetan plateau region in an idealized simulation," *Journal of Geophysical Research: Atmospheres*, vol. 119, no. 20, pp. 11543–11561, 2014.
- [10] Y. Chen, Y. Li, and T. Zhao, "Cause analysis on eastward movement of southwest China vortex and its induced heavy rainfall in south China," *Advances in Meteorology*, vol. 2015, Article ID 481735, 22 pages, 2015.
- [11] R. Zhong, L. Zhong, L. Hua, and S. Feng, "A climatology of the southwest vortex during 1979–2008," *Atmospheric and Oceanic Science Letters*, vol. 7, no. 6, pp. 577–583, 2014.
- [12] J. Fan and K. Chen, "Statistical analysis of the characteristics of the southwest vortex with/without the existing of typhoon," *Plateau Meteorology*, vol. 38, no. 4, pp. 744–755, 2019, in Chinese.
- [13] Y. Ye and G. Li, "Statistics characteristics and the abnormal development of flow pattern of the southwest vortex in recent 61 summer half year," *Plateau Meteorology*, vol. 35, no. 4, pp. 946–954, 2016, in Chinese.
- [14] Z. M. Chen and W. B. Min, *Research Progress of Theory of the Second Tibet Plateau Scientific Experiments*, China Meteorological Press, Beijing, China, 2000.
- [15] G. X. Shen and G. B. He, "The observed facts analysis of southwest vortex from 2000 to 2007," *Plateau and Mountain Meteorology Research*, vol. 28, no. 4, pp. 59–65, 2008, in Chinese.
- [16] D. Mu and Y. Q. Li, "Statistical characteristics summary of the southwest China vortex," *Journal of Arid Meteorology*, vol. 35, no. 2, pp. 175–181, 2017, in Chinese.
- [17] Z. S. Wang, Y. H. Wang, and Y. G. Liang, *Research on Science and Technology, Operational Experiments and Atmospheric*

- Dynamics of Rainstorm*, China Meteorological Press, Beijing, China, 1996.
- [18] Z. M. Chen, W. B. Min, and C. G. Cui, "New advances in southwest China vortex research," *Plateau Meteorology*, vol. 23, no. 1, pp. 1–5, 2004, in Chinese.
- [19] Q. Xu, G. D. Hoke, J. Liu-Zeng, L. Ding, W. Wang, and Y. Yang, "Stable isotopes of surface water across the Longmenshan margin of the eastern Tibetan plateau," *Geochemistry, Geophysics, Geosystems*, vol. 15, no. 8, pp. 3416–3429, 2014.
- [20] D. F. Parrish and J. C. Derber, "The national meteorological center's spectral statistical-interpolation analysis system," *Monthly Weather Review*, vol. 120, no. 8, pp. 1747–1763, 1992.
- [21] F. Karbou, F. Rabier, J.-P. Lafore, J.-L. Redelsperger, and O. Bock, "Global 4DVAR assimilation and forecast experiments using AMSU observations over land. Part II: impacts of assimilating surface-sensitive channels on the African monsoon during AMMA," *Weather and Forecasting*, vol. 25, no. 1, pp. 20–36, 2010.
- [22] Z. Liu, C. S. Schwartz, C. Snyder, and S.-Y. Ha, "Impact of assimilating AMSU-A radiances on forecasts of 2008 Atlantic tropical cyclones initialized with a limited-area ensemble Kalman filter," *Monthly Weather Review*, vol. 140, no. 12, pp. 4017–4034, 2012.
- [23] H. Lawrence, N. Bormann, Q. F. Lu, A. J. Geer, and S. J. English, "An evaluation of FY-3C MWS-2 at ECMWF," EUMETSAT/ECMWF Fellowship Programme Research Report (Report 37), European Centre for Medium-Range Weather Forecasts, Reading, UK, 2015.
- [24] D. P. Dee, "Variational bias correction of radiance data in the ECMWF system," in *Proceedings of the ECMWF Workshop on Assimilation of High Spectral Resolution Sounders in NWP*, vol. 28, pp. 97–112, Reading, UK, July 2004.
- [25] T. Auligné, A. P. McNally, and D. P. Dee, "Adaptive bias correction for satellite data in a numerical weather prediction system," *Quarterly Journal of the Royal Meteorological Society*, vol. 133, no. 624, pp. 631–642, 2007.
- [26] D. Barker, X.-Y. Huang, Z. Liu et al., "The weather research and forecasting model's community variational/ensemble data assimilation system: WRFDA," *Bulletin of the American Meteorological Society*, vol. 93, no. 6, pp. 831–843, 2012.
- [27] N. Bormann and P. Bauer, "Estimates of spatial and inter-channel observation-error characteristics for current sounder radiances for numerical weather prediction. I: methods and application to ATOVS data," *Quarterly Journal of the Royal Meteorological Society*, vol. 136, no. 649, pp. 1036–1050, 2010.
- [28] N. Bormann, A. Collard, and P. Bauer, "Estimates of spatial and interchannel observation-error characteristics for current sounder radiances for numerical weather prediction. II: application to AIRS and IASI data," *Quarterly Journal of the Royal Meteorological Society*, vol. 136, no. 649, pp. 1051–1063, 2010.
- [29] G. Thompson, P. R. Field, R. M. Rasmussen, and W. D. Hall, "Explicit forecasts of winter precipitation using an improved bulk microphysics scheme. Part II: implementation of a new snow parameterization," *Monthly Weather Review*, vol. 136, no. 12, pp. 5095–5115, 2008.
- [30] M. J. Iacono, J. S. Delamere, E. J. Mlawer, M. W. Shephard, S. A. Clough, and W. D. Collins, "Radiative forcing by long-lived greenhouse gases: calculations with the AER radiative transfer models," *Journal of Geophysical Research Atmospheres*, vol. 113, no. 13, 2008.
- [31] M. Tiedtke, "A comprehensive mass flux scheme for cumulus parameterization in large-scale models," *Monthly Weather Review*, vol. 117, no. 8, pp. 1779–1800, 1989.
- [32] C. Zhang, Y. Wang, and K. Hamilton, "Improved representation of boundary layer clouds over the southeast pacific in ARW-WRF using a modified tiedtke cumulus parameterization scheme," *Monthly Weather Review*, vol. 139, no. 11, pp. 3489–3513, 2011.
- [33] Z. I. Janjic, "The step-mountain eta coordinate model-further developments of the convection, viscous sublayer, and turbulence closure schemes," *Monthly Weather Review*, vol. 122, no. 5, pp. 927–945, 1994.
- [34] F. Chen and J. Dudhia, "Coupling an advanced land surface-hydrology model with the penn state-NCAR MM5 modeling system. Part I: model implementation and sensitivity," *Monthly Weather Review*, vol. 129, no. 4, pp. 569–585, 2001.
- [35] D. Xu, J. Min, F. Shen, J. Ban, and P. Chen, "Assimilation of MWS radiance data from the FY-3B satellite with the WRF hybrid-3DVAR system for the forecasting of binary typhoons," *Journal of Advances in Modeling Earth Systems*, vol. 8, no. 2, pp. 1014–1028, 2016.
- [36] Z. Xian, K. Chen, and J. Zhu, "All-sky assimilation of the MWS-2 observations and evaluation the impacts on the analyses and forecasts of binary typhoons," *Journal of Geophysical Research: Atmospheres*, vol. 124, no. 12, pp. 6359–6378, 2019.